Journal of Materials Chemistry A

ROYAL SOCIETY OF CHEMISTRY

PAPER

View Article Online
View Journal | View Issue

Cite this: J. Mater. Chem. A, 2025, 13, 26389

Visible lithiation gradients of bulk MoS_2 in lithium-ion coin cells†

Alexandar D. Marinov, [ab] Ami R. Shah, [a] Christopher A. Howard [c] and Patrick L. Cullen *[d]

Received 20th March 2025
Accepted 4th July 2025

DOI: 10.1039/d5ta02290h

rsc.li/materials-a

Molybdenum disulfide (MoS_2) is sought out to replace graphite as the negative electrode in lithium-ion batteries (LIBs), due to the higher theoretical capacity of bulk MoS_2 (670 mAh g^{-1}) and its natural abundance. However, upon deep discharge (0.01 V) MoS_2 suffers from rapid loss of performance. To further the understanding of the MoS_2 degradation mechanism, *ex situ* scanning electron microscopy (SEM), X-ray diffraction (XRD), Raman spectroscopy, and X-ray photoelectron spectroscopy (XPS) are carried out in the first lithiation and delithiation cycle. The study reveals that visible concentric coloured rings form in MoS_2 coin cells, whereby the electrode centre is underused unlithiated 2H MoS_2, the middle ring is partially lithiated 1T/2H Li_xMoS_2, and the outer ring experiences the full electrochemical pathway to form an amorphous product. Since lithiation inhomogeneities complicate MoS_2 lithiation mechanism studies in coin cells, we propose the use of thin (~10 μm) coatings and low current densities (~10 mA g^{-1}) to enable uniform lithiation.

Introduction

With the ever-growing global impact of humankind's reliance on fossil fuels[1] and the political disruption of the global supply chains for critical energy storage materials,[2] many countries have become dependent on the decisions of a few key exporters to meet their climate goals. As the global community aims to transition away from fossil fuel dependency, the demand and development of long range low-cost electric vehicles (EVs) is surging.[3] However, to compensate for lithium-ion battery (LIB) grade graphite powder supply chains being used as political leverage, high energy density materials with established large-scale supply-chains (~5280 T y^{-1} in 2020),[4] that can easily be inserted into current LIB manufacturing lines to diversify the anode side graphite monopoly in LIBs,[5] are becoming of greater scientific and societal interest.[6]

Molybdenum disulfide (MoS_2) is a heavily researched transition metal dichalcogenide, involved in LIB research since the 1980s.[7] From 2010 onwards, research involving MoS_2 as an anode in LIBs has expanded significantly[6] due to the higher theoretical capacity of MoS_2 (670 mAh g^{-1})[8] calculated for a four-electron pathway relative to the commercially successful graphite (360 mAh g^{-1}). However, MoS_2 suffers from poor cycling stability,[8–14] unless synthesised with a small particle size, special morphology, or combined in a carbon-based composite.[15–18]

Experimental MoS_2 LIBs are typically cycled under constant current densities (~100 mA g^{-1}) within a shallow (3.00–0.80 V) or deep (3.00–0.01 V) discharge voltage window *vs.* a Li^+/Li counter electrode.[8,10–14] In the shallow case, the commercial MoS_2 material reversibly intercalates and deintercalates lithium[8,9,19–21] (eqn (1)) achieving a stable capacity of 135 mAh g^{-1} at the 100th cycle.[8] The material characterisation data from *ex situ*, *in situ*, and *operando* studies with X-ray diffraction (XRD),[8,9,19–21] Raman spectroscopy,[8,20] and Mo K-edge, Mo L-edge, or S K-edge X-ray absorption (XAS)[8,9,21] are conclusive that the MoS_2 crystal structure is retained, despite some irreversibly trapped lithium and slight altering of the structure *via* lowered crystallinity.[8,9,19–21]

If deep discharge is employed the commercial MoS_2 initial cycles display a high capacity (694 mAh g^{-1}) that recedes within the first 100 cycles to 180 mAh g^{-1}.[8] During the first discharge (lithiation) (Fig. 1), following the Li_xMoS_2 lithiation plateau A at ~0.8 V [19] it is widely agreed that plateau B at ~0.4 V is the conversion reaction of Li_xMoS_2 into amorphous Li_2S and elemental Mo metal[8–10,12,13,19,21–28] (eqn (2)). This has been confirmed with *ex situ* and *in situ* high resolution transmission electron microscopy (HRTEM),[12,15,22,24,27–30] Raman spectroscopy,[8,10,27,29] XRD,[8,9,19,28] and S and Mo edge XAS.[8,27–29] Additionally, following deep discharge a gel-like layer develops across

[a]Electrochemical Innovations Laboratory (EIL), Department of Chemical Engineering, University College London, London, WC1E 6BT, UK

[b]CIC EnergiGUNE, Basque Research and Technology Alliance (BRTA), Alava Technology Park, Albert Einstein 48, 01510 Vitoria-Gasteiz, Spain

[c]Department of Physics & Astronomy, University College London, London, WC1E 6BT, UK

[d]School of Engineering and Materials Science, Queen Mary University, London, E1 4NS, UK. E-mail: p.cullen@qmul.ac.uk

† Electronic supplementary information (ESI) available. See DOI: https://doi.org/10.1039/d5ta02290h

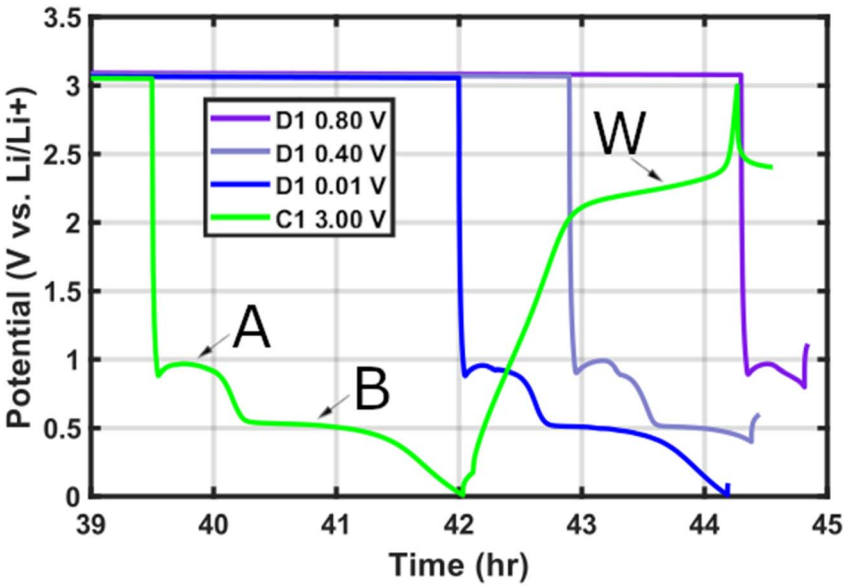

Fig. 1 Galvanostatic first cycle discharge (lithiation) and charge (delithiation) of MoS_2 electrode (~36 μm thick and 15 mm in diameter) coin cells performed at a constant current density ~200 mA g^{-1}. The cells are opened after achieving the desired cutoff voltage (D1 0.80 V, D1 0.40 V, D1 0.01 V, and C1 3.00 V).

the electrode surface as seen with scanning electron microscopy (SEM).[8–10,31]

However, upon first charge (delithiation) the literature sources begin to deviate from one another over the reaction taking place at plateau W (~2.3 V)[8] (Fig. 1). The leading MoS_2 deep discharge mechanism hypotheses consider: (i) reversible formation and conversion of MoS_2 and Li_2S + Mo on every charge and discharge,[10,12,15,24,27,32,33] respectively (eqn (3)). (ii) Irreversible formation of Li_2S + Mo during the first discharge, followed by Li–S chemistry (Li_2S/Li + S_8) operation in all subsequent cycles[8,13,19,22,29,34–37] (eqn (4)). (iii) Mixed mechanism operation that considers simultaneous reversible MoS_2 formation and Li–S chemistry.[28,38,39] (iv) Surface limited gel-layer passivation of the electrode beyond the 50th cycle after initial mixed mechanism operation.[10]

$$MoS_2 + xLi^+ + xe^- \rightleftharpoons Li_xMoS_2 \quad (1)$$

$$Li_xMoS_2 + (4 - x)Li^+ + (4 - x)e^- \rightarrow xLi_2S + Mo \quad (2)$$

$$Mo + 2Li_2S \rightleftharpoons MoS_2 + 4Li^+ + 4e^- \quad (3)$$

$$8Li_2S \rightleftharpoons S_8 + 16Li^+ + 16e^- \quad (4)$$

For bulk MoS_2 extracted through mining and refinement or synthetically produced MoS_2 to be commercially viable for LIBs, it is necessary to maintain the material's high initial cycle capacities long-term by stabilising the reaction pathway without incurring exceptional production or manufacturing costs. To move towards this goal, it is crucial to understand the lithiation and material degradation mechanism of bulk MoS_2 in the pivotal early LIB cycles.

Therefore, herein we lithiated MoS_2 electrodes (coating thickness ~12 μm, ~36 μm, and ~89 μm) to various depths of discharge (D1 0.80 V, D1 0.40 V, and D1 0.01 V) or charge (C1 3.00 V) in the first cycle, to observe the effects on the material coating. Visually, all coin cell electrodes displayed concentric coloured rings, which through *ex situ* characterisation with SEM, XRD, Raman spectroscopy, and XPS depth-profiling show a radial lithiation gradient favouring the electrode exterior. Whereby, the electrode centre remains almost pristine without signs of lithiation, suggesting a severe active material underuse in MoS_2 coin cells despite the specific capacity being only 27% short of the theoretical limit (670 mAh g^{-1}).[8]

Our findings highlight a MoS_2 lithiation inhomogeneity taking place in coin cells, which can greatly affect mechanism studies and showcases the multi-level reactions complicating the understanding of MoS_2. To tackle the lithiation inhomogeneity, we recommend the use of thin films (~10 μm) of commercial bulk MoS_2 for future mechanism studies and lower current densities (~10 mA g^{-1}) to enable a uniform electrochemical reaction across the electrode and facilitate cross-study comparison.

Experimental details

Materials

Top-down precursor MoS_2 (CAS: 1317-33-5) with an average flake size of ~6 μm and a maximum size of 40 μm, also referred to as commercial or bulk MoS_2 (98+%), was purchased from Sigma-Aldrich. Carbon black conductive additive (Super P™, 99+%) was purchased from Alfa Aesar (CAS: 1333-86-4). PVDF with the commercial name Solef® 5130 was purchased from Solvay®. Copper foil was purchased from Cambridge Energy Solutions, with an average thickness of 11 μm. Anhydrous *N*-methyl-2-pyrrolidone (NMP; CAS: 872-50-4) was purchased from Sigma Aldrich. 1 M $LiPF_6$ in EC/DMC (3 : 7 vol) LIB electrolyte was purchased from PuriEL under the commercial name of SoulBrain MI.

Electrode manufacture

Pristine MoS_2 battery electrodes were made by slurry-casting, with a coating composition of 80 : 10 : 10 wt% of MoS_2, Super P, and PVDF. In a typical process, 3.0 g of PVDF are mixed with 57 mL of NMP (≈58.7 g) and stirred for 24 hours at 400 rpm, to make a 5 wt% PVDF/NMP solution. 500 mg of MoS_2 powder, 63 mg of Super P powder, and 1250 mg of PVDF (5 wt%)/NMP solution (≈63 mg PVDF) are added to a plastic tub.

The mixture is stirred using a planetary mixer (THINKY ARE-250), with a two-step process. The first step is 0.5 min at 500 rpm to degas the mixture, whilst the second step is 15 min at 1500 rpm to homogenise the slurry. Additional NMP can be added between mixing iterations, to adjust the consistency. The goal is a paint-like smooth flowing slurry.

The slurry is coated onto clean copper foil using a doctor blade and an automatic film coater (Elcometer 4340). The formed electrode is dried on a hot plate at 60 °C until the coating is visibly dry. The coating thickness is measured with a Mitutoyo height gauge. Five points across the electrode surface are sampled to attain an average thickness. In some cases, individual coin cell electrodes are measured as reported in Table SI 1.†

Coin cell assembly & testing

Electrode discs of 15 mm diameter are punched out with a press. The average mass of blank copper 15 mm discs is ∼15.3 mg (∼8.70 mg cm^{-2}), whereas the average active mass loading of the thin (∼12 μm), medium (∼36 μm), and thick (∼89 μm) electrodes are ∼1.11 mg cm^{-2}, ∼3.43 mg cm^{-2}, and ∼8.15 mg cm^{-2}, respectively. The electrode discs are dried at 60 °C for 24 hours in a Buchi tube furnace and taken directly into an inert argon glovebox atmosphere (O_2, H_2O <0.5 ppm).

Individual electrodes are weighed (Kern ABT 120-4NM) inside the glovebox (Table SI 1†) and assembled in Hohsen CR2032 coin cells, using a 19 mm diameter and 25 μm thick Celgard separator, 100 μL of 1 M $LiPF_6$ in EC/DMC (3 : 7 vol) electrolyte, a lithium foil counter (MTI Corporation) with a larger diameter than the working electrode, and a 1 mm thick spacer.

Coin cells were cycled using a BioLogic BCS cycler, between the voltages of 3.00–0.80 V, 0.40 V, and 0.01 V, at current densities of 100–200 mA g^{-1}. Coin cells were taken off the cycler and disassembled inside an argon-filled glovebox within 20 min of cycle termination. The only exception is the ∼12 μm C1 3.00 V cell, which was opened at a stable voltage of 2.46 V. Working electrodes were washed with clean di-methoxyethane (DME) to remove remnants of $LiPF_6$ salt. The counter electrodes were not washed.

All cell capacities (mAh g^{-1}) provided are normalised by the mass of active material (80 wt%) in the electrode.

Material characterisation

All digital images were taken with a Google Pixel 3a camera, with *ex situ* samples and pristine lithium foil being photographed through the glovebox window.

SEM was conducted with a Zeiss EVO MA 10 SEM with a tungsten thermionic electron source and a scintillator-type Everhart–Thornley secondary electron detector. The accelerating voltage was set to 10 kV. Multicoloured *ex situ* sample strips were taken out of the inert glovebox atmosphere and transferred into the SEM within 2 min to minimise air exposure.

XRD was conducted in reflection geometry with a Bruker D2 Phaser benchtop diffractometer with a Cu source (30 kV and 10 mA) and scanned with a 50 s per degree exposure (1–80°). *Ex situ* samples were cut with scissors according to surface colour and attached with carbon tape onto the Si holder. XRD was carried out after several days of exposure to air and is therefore most prone to changes induced by oxygen and moisture.

Raman spectroscopy was conducted with a Renishaw InVia Reflex microscope with a 785 nm (300 mW) laser, operated at 1% power with a ×40 long distance working objective. The device is used with a 2400 L mm^{-1} diffraction grating giving a laser spot size of approximately 3 μm. Data collection is carried out with a multichannel charge-coupled device camera detector. *Ex situ* measurements were conducted air-free on multicoloured sample strips by using a custom glass holder with a Swagelok™ cap to create an air-tight seal.

XPS was conducted with a K-Alpha Thermo Fisher Scientific (Al Kα) spectrometer. Pristine powder and electrode samples were vacuum dried at 60 °C for 24 hours prior to XPS measurements. *Ex situ* electrodes were cut with scissors according to surface colour and loaded directly onto an air-free XPS transfer stage inside the glovebox. Ar^+ etching was conducted at a 3000 eV ion energy and a high ion current.

All XPS regions were fitted with a U2 Tougaard background in CasaXPS. The MoS_2 Mo^{4+} $3d_{3/2}$ peak was restricted by a separation of +3.1 eV, 66.7% area, and 110% FWHM relative to its major split orbit peak Mo^{4+} $3d_{5/2}$ for all phases. Similarly, the MoS_2 S^{2-} $2p_{1/2}$ peak was restricted by a separation of +1.16 eV, 50% area, and a 100% FWHM relative to its S^{2-} $2p_{3/2}$ split orbit peak. More detailed XPS fitting procedures can be found in Note II in the ESI.†

Results & discussion

Pristine electrodes are made by casting a slurry of commercial MoS_2 flakes (∼6 μm), carbon Super P, and PVDF binder with a common literature formulation of 80 : 10 : 10 wt% (Table SI 2†) with a doctor blade. The as-made electrodes display a greyish-blue hue (Fig. SI 1†), a flake-like morphology in SEM (Fig. SI 2†), crystalline MoS_2 XRD patterns (Fig. SI 3†), and 2H phase MoS_2 in Raman (Fig. SI 4†) and XPS spectra (Fig. SI 5†). Homogenous electrode coating thickness (Table SI 3†) and mass (Table SI 4†) is ensured by sample statistics.

The first cycle gives rise to a highly repeatable voltage profile (Fig. 1) with clear discharge plateaus A (0.96 V)[8,9,19,28,30,40] and B (0.51 V),[8,9,19,28,30,40] and a single charge plateau W (2.1–2.4 V).[8,9,19,28,30,40] The discharge profile is consistent irrespective of electrode thickness, only varying in the delivered first discharge specific capacity (Fig. SI 6†) as thin electrodes (∼12 μm) are favoured in terms of mass-based capacity[41] (∼785 mAh g^{-1}) relative to the thicker electrodes (∼36 μm; ∼487 mAh g^{-1} and

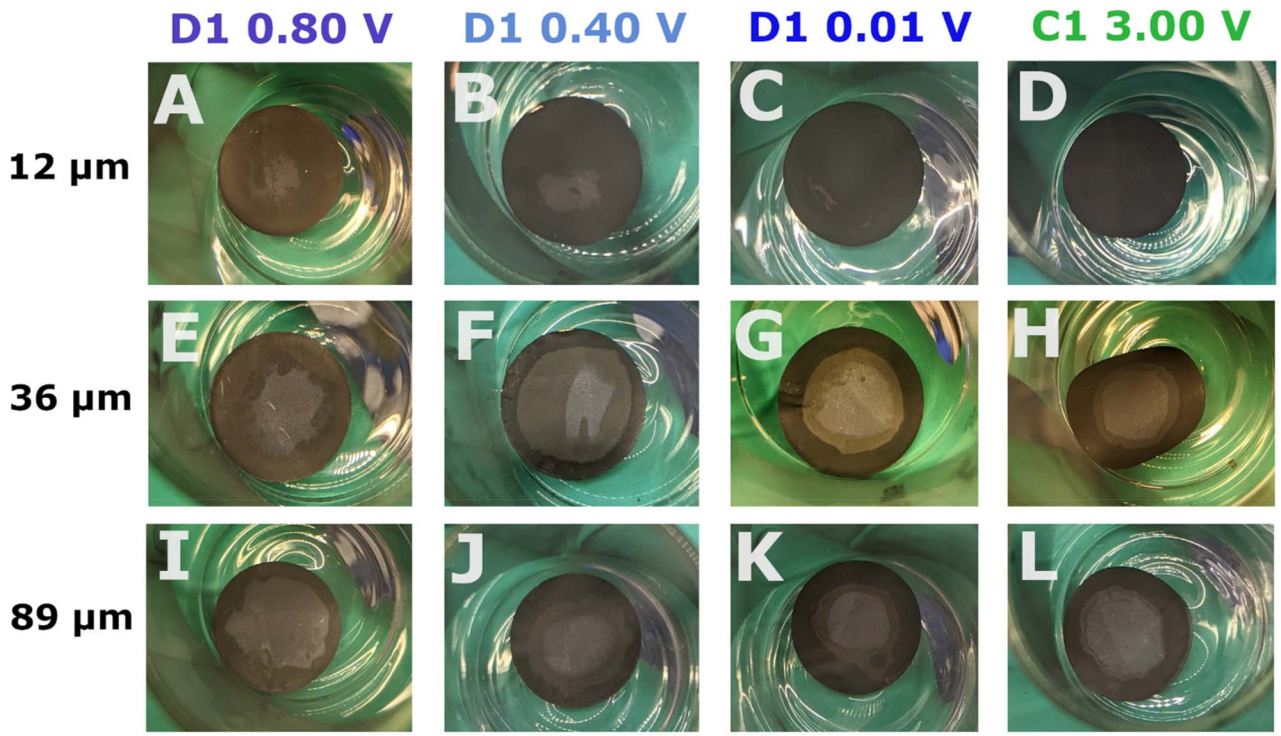

Fig. 2 Digital images of MoS_2 electrodes with a uniform diameter of 15 mm lithiated to D1 0.80 V, D1 0.40 V, and D1 0.01 V, or lithiated to D1 0.01 V and then delithiated to C1 3.00 V, at a constant current density of 100–200 mA g^{-1} in a lithium-metal half-cell, for varying electrode thicknesses of (A–D) ~12 μm, (E–H) ~36 μm, and (I–L) ~89 μm. The coin cells were disassembled within 20 minutes of achieving the desired voltage and the electrodes were washed with fresh DME to remove any electrolyte salt remnants. Only the ~12 μm C1 3.00 V cell was opened 38 hours after completion of its cycling protocol at a stable voltage of 2.46 V.

~89 μm; ~471 mAh g^{-1}). The long-term performance over 500 cycles of the different coating thicknesses is verified across 3 cells per thickness to ensure sample consistency (Fig. SI 7–SI 9†).

Upon opening coin cells on their first cycle within 20 minutes of achieving the desired voltage (Fig. 2), concentric coloured rings are observed across the working electrodes. The inhomogeneous colour distribution worsens as the electrode coating thickness increases (Fig. 2E–L), but nonetheless even the thin electrodes (~12 μm) are affected (Fig. 2A–D).

In most cases three rings are present across the electrode surface (Fig. 2), although in the shallow discharge (D1 0.8 V) the middle rings are extremely faint. Only in the thin (~12 μm) electrodes D1 0.01 V and C1 3.00 V the middle rings are absent altogether, as the electrodes become almost uniform in colour (Fig. 2C and D).

The lithium counter electrodes show varying degrees of lithium usage depending on the MoS_2 working electrode thickness (Fig. SI 10†). In contrast to the smooth pristine lithium (Fig. SI 11A†), the cycled counter electrodes display indications of lithium involvement. In the cells with the thin working electrodes, a roughening of the lithium surface occurs (Fig. SI 10†), whereas in the thicker electrode cells (≥36 μm) a darkening of the counter electrode surface takes place.

Notably, in the thicker MoS_2 cells the lithium darkening only occurs in the outer areas of the counter electrodes (Fig. SI 11†), matching the dark areas of the MoS_2 working electrodes. Suggesting, that the dark outer regions of the thicker MoS_2 working electrodes experience the greatest contact and interaction with the lithium counter electrodes.

On the other hand, the centre of the lithium counter electrodes appears similar to the pristine lithium metal (Fig. SI 11A†). Likewise, the inner most region of the cycled MoS_2 electrodes (Fig. SI 11†) appears similar to the pristine MoS_2 electrode (Fig. SI 1†). Suggesting, that the interior of the MoS_2 working electrode is increasingly underused as the electrode coating thickness increases (Fig. 2).

Cycling ~36 μm thick MoS_2 electrodes within the deep discharge voltage range for up to 50 cycles does not lead to the disappearance of the inhomogeneous concentric rings (Fig. SI 12†). Instead, the peculiar shapes appearing on the long-term cycled MoS_2 electrodes leave an identical dark imprint on their respective lithium counters (Fig. SI 12†). Therefore, strongly reinforcing the notion that electrochemical contact between the electrodes is the key reason for the colour inhomogeneity.

To facilitate *ex situ* material characterisation, we introduce the following nomenclature for the ~36 μm MoS_2 working electrodes, to differentiate the coloured rings based on the electrochemical plateaus A, B, and W (Fig. 1) preceding their observation (Fig. SI 13†), respectively. For instance, in the shallow discharge (D1 0.80 V) the outer ring is AX1, the middle ring is AX2, and the electrode centre is AX3. The same logic is applied to the D1 0.01 V (BX1–BX3) and C1 3.00 V (WX1–WX3) electrodes.

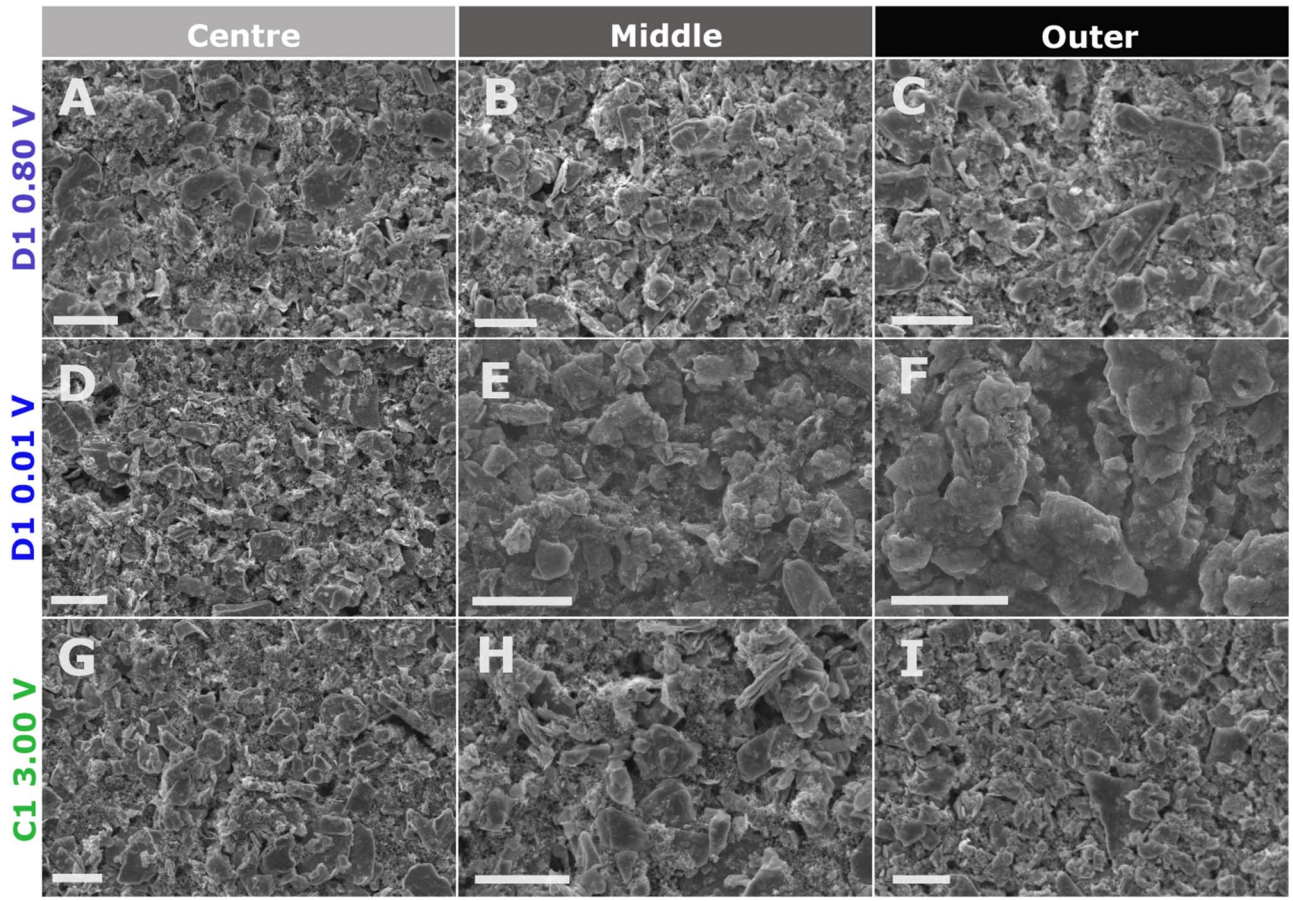

Fig. 3 *Ex situ* SEM of the (A–C) D1 0.80 V, (D–F) D1 0.01 V, and (G–I) C1 0.01 V ~36 μm thick MoS_2 working electrodes cycled in a lithium-metal half-cell at a current density of 200 mA g^{-1}. All scale bars are 10 μm.

SEM

We applied *ex situ* SEM to all multi-coloured areas of the cycled ~36 μm MoS_2 working electrodes to verify whether the electrode morphology changes based on lithiation and delithiation in the first cycle.

For the shallow discharge (D1 0.80 V), there is no change in the MoS_2 flake morphology (Fig. 3A–C) despite the visible change in the electrode colour (Fig. 2E). All three coloured rings (AX1–AX3) display the preserved MoS_2 flake morphology, as was observed in the pristine electrode (Fig. SI 2†).

Following a deep discharge (D1 0.01 V) a disparity in morphology takes place between the coloured rings (Fig. 3D–F). The electrode centre (BX3) retains the pristine electrode MoS_2 flake-like morphology (Fig. 3D). However, the middle ring (BX2) exhibits a mix of preserved pristine MoS_2 flakes (Fig. SI 14A†) and the formation of a gel-like layer[10,13,31,42] that covers the electrode surface (Fig. 3E and SI 14B†). Nevertheless, most of the middle ring surface contains the preserved flake morphology. Only the outer ring (BX1) is completely covered by the gel-like layer throughout and experiences the apparent disintegration of the MoS_2 flake structure (Fig. 3F and SI 15†).

The morphology of the fully delithiated electrode (C1 3.00 V) following a deep discharge (D1 0.01 V) exhibits only pristine MoS_2 flakes (Fig. 3G–I) across all three coloured rings (WX1–WX3) (Fig. 2). Surprisingly, the outer ring (Fig. 3I) has no gel-like layer presence despite its dark colour (Fig. 2L) and the preceding electrochemical plateau resulting in BX1 being entirely covered by the gel-like layer.[10,13,31,42] To the best of our knowledge, this is the first time that the removal of the MoS_2 gel-like layer has been demonstrated.

Despite, the appearance of the darkest colour alongside the formation of the gel-like layer in D1 0.01 V (BX1), the gel-like layer itself is not responsible for the dark colour. Since, in C1 3.00 V (WX1) the dark colour remains (Fig. 2H) despite the gel-like layer disappearing (Fig. 3I). It is also unlikely for the dark colour to be due to coin cell geometry, as in that case the dark colour would be observed across all states of discharge and charge for a given thickness. Therefore, the chemical reaction taking place in the outer ring at the lower voltages D1 (>0.40 V), where electrochemical contacting and the current experienced is greatest, is responsible for the dark colour in the outer ring.

XRD

To compare the crystallographic properties of the outer, middle, and central regions of each coin cell electrode, appropriate

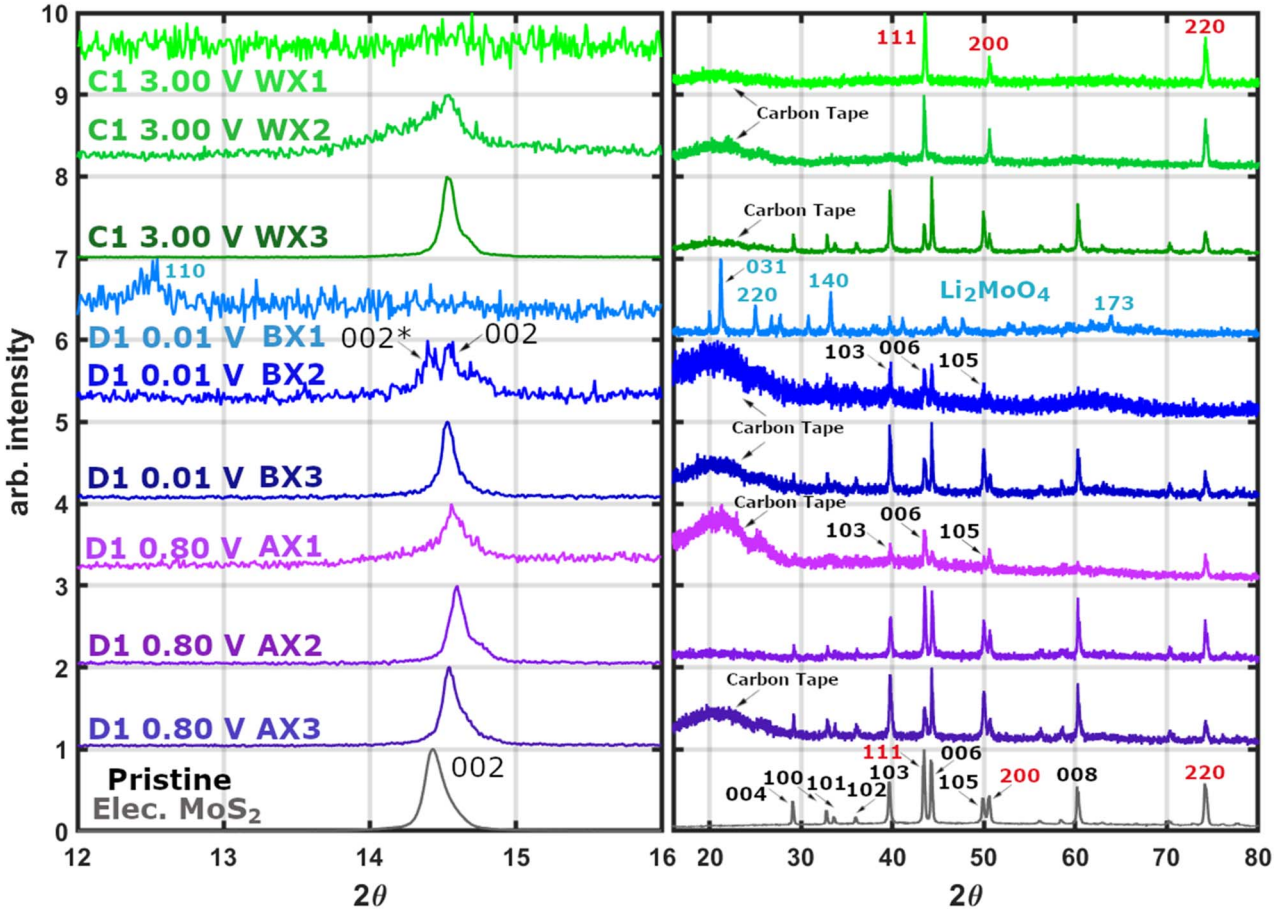

Fig. 4 *Ex situ* XRD (Cu source) of ~36 μm thick MoS_2 electrodes cycled to D1 0.80 V, D1 0.01 V, and C1 3.00 V in a lithium-metal half-cell at a current density of 200 mA g^{-1}. Black indices belong to MoS_2, red indices denote the copper current collector, and light blue indices identify Li_2MoO_4. Note, sample BX1 delaminated from the copper current collector and therefore does not have any copper peaks.

sections of each *ex situ* electrode were cut with scissors and studied with XRD.

The electrode centres AX3, BX3, and WX3 (Fig. 4) perfectly match the pristine MoS_2 electrode, despite having been present during lithiation/delithiation within a LIB. The only distinction between the pristine electrode and the cycled electrode centres, is the slight upshift in peak 2θ values due to the introduction of carbon tape beneath the samples (Fig. 4). Unfortunately, the Bruker D2 Phaser diffractometer cannot account for height calibration, but the copper current collector peaks also upshift by the same amount for similar values of 2θ (Fig. SI 16†), validating that the change in sample height is responsible for the diffraction pattern upshift and not a change in the material *d*-spacings.

The lack of change in the diffraction patterns of the *ex situ* electrode centres supports the visual observations from the working electrodes (Fig. 2) and the lack of involvement in their corresponding lithium metal counter electrode centres (Fig. SI 10†). Again, suggesting that the MoS_2 working electrode and lithium counter electrode centres are underused and do not participate in the lithiation mechanism.

The middle rings (AX2, BX2, and WX2) show significant variability based on the depth of discharge. The AX2 region of the shallow discharge retains the 2H MoS_2 character of the pristine electrode (Fig. 4), despite peaks reducing in intensity as the coating becomes irreversibly more amorphous as has been observed previously.[8,9,19,21,40]

However, the deep discharge BX2 region exhibits a large change with most of the 2H MoS_2 indices (103, 006, and 105) becoming extremely faint whilst the rest of the higher angle MoS_2 peaks vanish altogether.[8,9] Even the intensity of the dominant 002 MoS_2 index severely decreases, noticeable by the relative increase in the constant copper current collector indices (Fig. SI 17†).

At the same time, the dominant 002 MoS_2 index splits into a doublet (Fig. 4), whereby the downshifted 002* index indicates the expanded *d*-spacing of MoS_2 due to lithium intercalation[8,9,19,40] (Li_xMoS_2). In the case of the charged WX2 region, all MoS_2 diffraction peaks vanish (Fig. 4) aside from a heavily decreased intensity 002 index (Fig. SI 17†).

In the outer most coloured rings (AX1, BX1, and WX1), the shallow discharge AX1 region retains the 002, 103, and 105

MoS2 indices (Fig. 4), although their intensity is severely reduced as much of the 2H MoS2 crystalline structure is lost (Fig. SI 18†). Nevertheless, the observations are in agreement with previous shallow discharge XRD studies.[8,9,19,40]

At the same time, the deep discharge ring BX1 is completely void of any MoS_2 peaks, does not contain any copper current collector indices as the coating delaminated from the substrate, and is instead identified as Li_2MoO_4 (Fig. 4). However, it should be noted that exposure of lithiated MoS_2 to atmospheric conditions will result in the formation of Li_2MoO_4 crystals on the electrode surface (see Note I†), which are not present immediately following LIB operation (Fig. SI 19–SI 21†).

On the other hand, the charged electrode ring WX1 is completely void of any material indices aside from the copper current collector peaks (Fig. 4). This is unexpected from the preserved flakes observed with SEM (Fig. 3G–I).

Due to the large degree of amorphousness of the outer ring, especially following deep discharge, no conclusive outcome can be established. Previous studies have also struggled to support proposed mechanisms conclusively with solely XRD.[22,36,37]

Herein, the stark crystallographic difference between the coloured regions within a single coin cell electrode have been highlighted. This is especially problematic, as depending on which region of the electrode is analysed, strongly opposing lithiation mechanism conclusions can be reached in the absence of sufficient information.

Raman spectroscopy

To investigate the multi-coloured electrode surfaces, cycled MoS_2 electrodes are cut into tri-coloured strips and studied with air-free *ex situ* Raman spectroscopy by using a custom Swagelok sample holder.

The electrode centres (AX3, BX3, and WX3) clearly demonstrate there is no difference between the pristine electrode and the cycled centres irrespective of the cutoff voltage used (Fig. 5 and SI 21–SI 24†). Strongly reinforcing the previous data from SEM and XRD, validating that the electrode centres do not participate in lithiation/delithiation.

Within the middle coloured rings (AX2, BX2, and WX2), the shallow discharge (AX2) is the only segment that retains some degree of 2H phase MoS_2 (Fig. 5 and SI 25†) with the presence of the $E^1_{2g}(\Gamma)$ (382 cm^{-1}) and $A_{1g}(\Gamma)$ (407 cm^{-1}) modes, alongside the rise of the 1T phase lower end TA(M) (149 cm^{-1}) and $E_{1u}(M)$–TA(M) (205 cm^{-1}) modes associated with the formation of lithiated[8,40] Li_xMoS_2. At the same time, the low intensity higher shift (500–900 cm^{-1}) pristine 2H MoS_2 modes vanish in all three states.

On the other hand, the deep discharge middle BX2 ring only displays 1T phase Li_xMoS_2 peaks (Fig. 5 and SI 26†), exhibiting the clearest 1T signal out of all regions scanned. Whilst the charge WX2 region shows only a faint 1T presence (Fig. 5 and SI 27†).

For the outer most rings (AX1, BX1, and WX1), the deep discharge (BX1) and charge (WX1) areas are completely void of any MoS_2 presence (Fig. 5 and SI 28, SI 29†). Only the shallow discharge ring AX1 displays Li_xMoS_2 Raman modes (Fig. 5 and SI 30†), with the presence of weak mixed phase 1T/2H MoS_2 peaks as were observed previously in AX2 (Fig. 5 and SI 25†). Nevertheless, out of all positions scanned in AX1, the majority exhibited only 1T peaks (Fig. SI 30†), indicating a greater degree of lithiation than in the middle ring AX2 (Fig. SI 25†).

The findings agree with previous studies showing the formation of Li_xMoS_2 during shallow discharge,[8,10,27,40] followed by the disappearance of Raman signal during deep discharge.[10,27] However, in contrast to previous studies after charge the electrochemically active regions (WX2 and WX1) do not reversibly recover MoS_2 [10,27] nor irreversibly form sulfur.[8,29]

XPS

To gain elemental insight into the multi-coloured electrode surfaces, air-free *ex situ* XPS is carried out by cutting coloured sections from the cycled electrodes with scissors and using a custom air-tight sample transfer stage.

XPS analysis clearly denotes all three electrode centres (AX3, BX3, and WX3) as 2H phase MoS identified through high intensity Mo 3d and S 2p peaks closely resembling the pristine electrode (Fig. 6 and SI 31, SI 32†). The AX3 and BX3 peaks upshift to higher binding energies (229.6 eV & 162.4 eV) than the pristine electrode (229.4 eV & 162.2 eV), whereas the WX3 peaks remain almost unchanged (229.3 eV & 162.1 eV).

However, in all three electrode centres the binding energy separation (ΔBE) between the Mo $3d_{5/2}$ A and S $2p_{3/2}$ A peaks (67.18 eV) is conserved $\sim\pm0.02$ eV, indicating that any changes in peak binding energies are due to either surface charging within the XPS spectrometer[43] or calibration differences. At the same time, the charge centre (WX3) peaks broaden out significantly and decrease in intensity (FWHM 1.04 eV) relative to the pristine electrode (FWHM 0.85 eV), indicating a slight increase in material disorder[44] following exposure to the LIB environment for a full cycle.

Even though the central Mo 3d and S 2p peaks remaining relatively unchanged (Fig. 6), the surface electrolyte interphase (SEI) layer related species fluorine, oxygen, and carbon dominate the XPS survey spectra (Fig. SI 32†). Therefore, an SEI layer develops within the LIB cell even in the absence of MoS_2 activity due to poor electrode contacting.

Irrespective of depth of discharge, the middle electrode rings (AX2, BX2, and WX2) exhibit a binding energy downshift for both the Mo 3d and S 2p regions (Fig. 6 and SI 33†), with dominant 1T phase MoS_2 peaks at approximately 228.4 eV (Mo $3d_{5/2}$) and 161.5 eV (S $2p_{3/2}$) due to the formation of Li_x-MoS_2.[6,15,45–47] In all middle rings, weaker 2H phase MoS_2 peaks can also be found on the electrode surface, highlighting that lithiation in the middle rings is incomplete with some of the active material remaining unused.

Additionally, the middle ring Mo 3d and S 2p peaks partially shift in binding energy (229.5 eV & 162.1 eV) relative to the pristine electrode (229.4 eV & 162.2 eV) and possess a ΔBE (67.43 eV) with a greater variation ($\pm$0.17 eV) than the central regions. This is caused by the difficulty in fitting low intensity XPS signals with an increased number of MoS_2 phases (Fig. 6). The MoS_2 and Li_xMoS_2 peak intensities in the middle rings are significantly lower than the pristine electrode and the electrode centres (Fig. 6), exhibiting a sharp reduction in MoS_2 presence

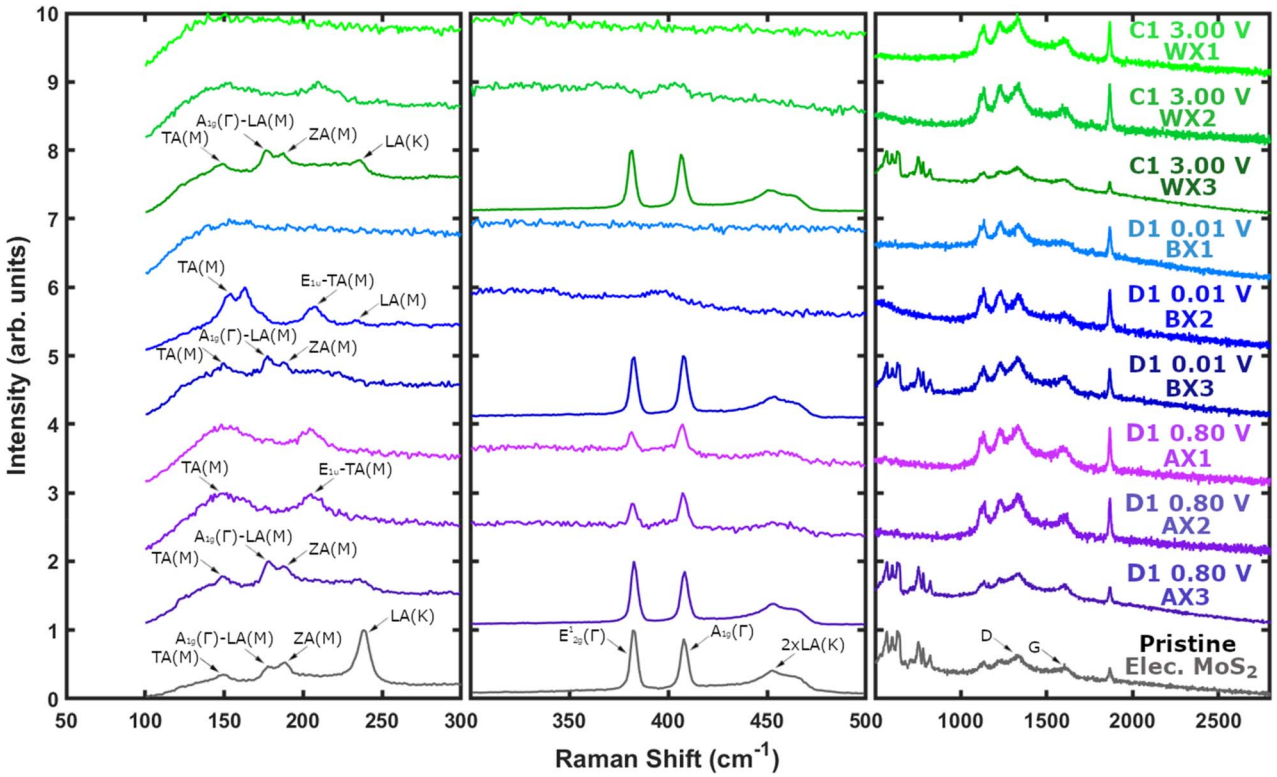

Fig. 5 *Ex situ* air-free Raman spectroscopy (785 nm laser) of ~36 μm thick MoS_2 electrodes cycled to D1 0.80 V, D1 0.01 V, and C1 3.00 V in a lithium-metal half-cell at a current density of 200 mA g^{-1}.

in the middle ring in favour of SEI growth through fluorine, oxygen, carbon, and lithium species (Fig. SI 34†).

Within the outer ring (AX1, BX1, and WX1), the XPS signal varies greatly between the three states of discharge/charge (Fig. 6 and SI 35, SI 36†). The shallow discharge AX1 ring closely resembles the middle ring AX2, with a strong 1T phase MoS_2 presence but expresses a reduction in 2H phase MoS_2. Therefore, suggesting that greater electrode contacting in the outer region of the shallow cell results in a higher degree of Li_xMoS_2 and less underused active material remaining as 2H MoS_2.

The deep discharge BX1 region is void of sufficient Mo or S presence to garner sample fitting (Fig. 6), showcasing an absence of MoS_2, Mo, or Li_2S[8–10,12,13,19,21–28] on the electrode surface. This finding is confirmed by scanning two additional locations on the sample surface for consistency (Fig. SI 35†). Therefore, neither supporting the reversible[10,12,15,24,27,32,33] nor irreversible[8,13,19,22,29,34–37] mechanism hypotheses.

Following charge, the outer region (WX1) exhibits presence of 2H phase MoS_2 (229.8 eV), 1T MoS_2 (228.5 eV), MoO_3 (231.6 eV), and sulphates (SO_x ~166–169 eV) (Fig. 6 and SI 35†). No significant amount of elemental sulfur (~163.9 eV)[48,49] can be found in WX1 to support the irreversible mechanism hypothesis, nor is the MoS_2 presence strong enough to warrant justification for reversible formation. Overall, the surface WX1 contribution of both molybdenum and sulfur compounds is minimal, collectively Mo + S account for 2.1 at%, whilst the SEI species fluorine (13.7 at%), oxygen (18.3 at%), carbon (45.6 at%), and lithium (20.0 at%) dominate the surface layer (Fig. SI 36†).

Etching of the cycled electrodes results in the modulation of the sample, due to the preferential removal[44,50–55] of sulfur from MoS_2 (Fig. SI 37 and SI 38†). However, in all rings and regions etching reveals the presence of MoS_2 below the surface (Fig. SI 37 and SI 38†). Even the most electrochemically active outer region (BX1), shows noticeable amounts of MoS_2 underneath the surface. Therefore, suggesting that MoS_2 remains inactive during the first cycle not just radially but with depth as well.

Unfortunately, the phase and composition of the unearthed MoS_2 cannot be established as the Mo 3d and S 2p binding energies downshift across all electrode regions (Fig. SI 37 and SI 38†) as a result of argon ion bombardment.[44,50–55] Hence, it remains unknown whether the material is 2H or 1T prior to etching.

Overall, XPS confirms the Raman spectroscopy observation that MoS_2 lithiates progressively further moving radially outwards from the electrode centre (Fig. 6), due to the improved electrochemical contacting between the working electrode and the lithium counter electrode. In the shallow discharge this results in a greater presence of Li_xMoS_2 relative to inactive 2H MoS_2, whereas in the deep discharge MoS_2 vanishes altogether and does not recover significantly after charge.

It is important to highlight, that even in the pristine electrode fluorine (18.0 at%), oxygen (4.0 at%), and carbon (58.3 at%) make up most (80.3 at%) of the electrode surface (MoS_2; 16.4 at%), whereby their contribution increases further with the

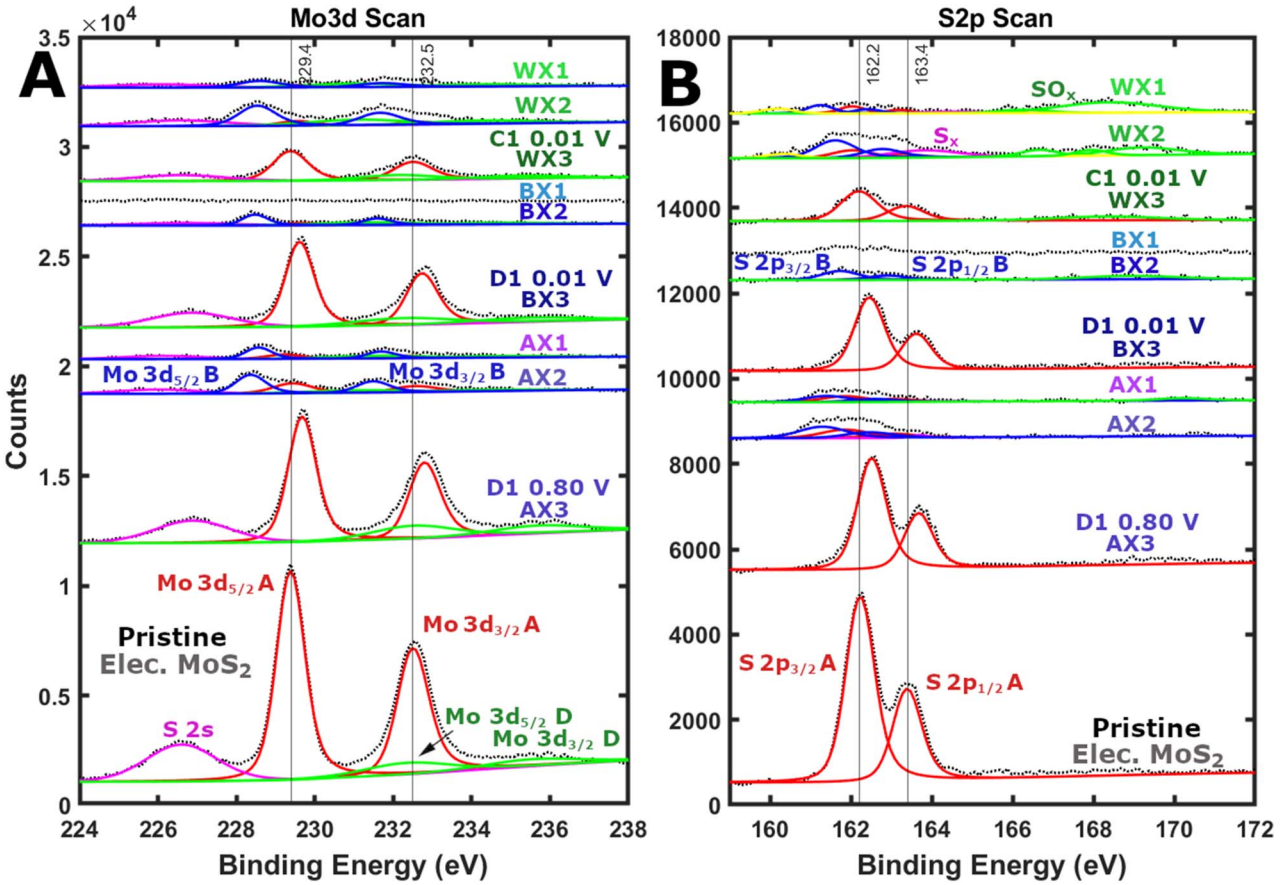

Fig. 6 *Ex situ* air-free XPS of ~36 μm thick MoS_2 electrodes cycled to D1 0.80 V, D1 0.01 V, and C1 3.00 V in a lithium-metal half-cell at a current density of 200 mA g^{-1}. (A) Mo 3d region and (B) S 2p region.

first cycle when considering the addition of lithium (6.6–25.4 at%) to the SEI species (88.9–100.0 at%) and the severe reduction of the MoS_2 presence (0.0–5.2 at%). Therefore, it is highly probably that the unstable development of an SEI layer might be a leading cause for long-term performance deterioration[10] (Fig. SI 7 and SI 12†), as suggested by the observation of deposition (Fig. 2F) and removal (Fig. 2I) of the gel-like layer on discharge and charge, respectively.

Surplus capacity

Fig. 7 provides an overarching summary of all the information gathered from *ex situ* material characterisation (SEM, XRD, Raman, and XPS). Regardless of the depth of discharge or state of charge, the first cycle electrode centre remains as pristine 2H MoS_2 identified through morphology, crystallinity, phase, and chemical signature.

Within the middle rings (AX2, BX2, and WX2) MoS_2 is partially lithiated with some amount remaining as 2H MoS_2, whilst depth profiling reveals the existence of MoS_2 underneath all surface layers irrespective of voltage. Hence, for a medium thick (~36 μm) MoS_2 electrode in a CR2032 coin cell, a significant percentage of the active material acts as dead mass.

Therefore, despite the MoS_2 active mass loading of 3.43 mg cm^{-2} a smaller fraction of the active material contributes to the 102 mAh g^{-1} and ~487 mAh g^{-1} capacity delivered within the first shallow (3.00–0.80 V) and deep discharge (3.00–0.01 V), respectively.

Part of the added deep discharge capacity can be attributed to the consumption of electrolyte to form the gel-like layer observed in BX1 (Fig. 2F), but nonetheless a significant amount of MoS_2 in the electrode remains non-lithiated or partially lithiated (Li_xMoS_2 ~100 mAh g^{-1}) (Fig. 6). Hence, suggesting there exists a source of surplus capacity enabling the active MoS_2 in the outer ring to exceed its one-electron shallow (167 mAh g^{-1}) or four-electron deep discharge (670 mAh g^{-1})[8] pathway theoretical capacity.

To reduce the impact of MoS_2 lithiation inhomogeneity within mechanism studies, we suggest the use of thin electrode coatings (~10 μm) cycled at low current densities (~10 mA g^{-1}), and at least *ex situ* visual colour homogeneity validation. Low loadings and currents will enable the active material to fully lithiate (Fig. 2A–D), achieving the full storage capacity, facilitating the identification of the electron transfer number required.

Additionally, utilising a widely available commercial bulk MoS_2 material will enable for studies to be replicable, directly comparable, and explored further across different research facilities.

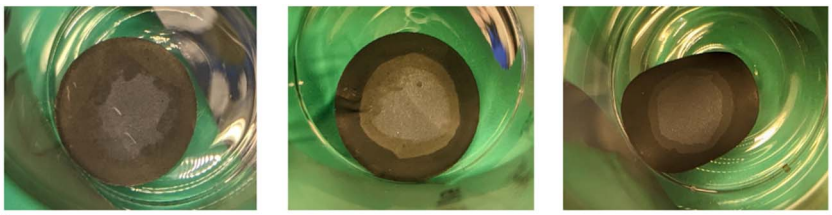

		D1 0.80 V	D1 0.01 V	C1 3.00 V
Centre	SEM	Flake	Flake	Flake
	XRD	MoS_2	MoS_2	MoS_2
	Raman	2H MoS_2	2H MoS_2	2H MoS_2
	XPS	2H MoS_2	2H MoS_2	2H MoS_2
Middle	SEM	Flake	Flake/Fuzzy	Flake
	XRD	MoS_2	~ MoS_2/Li_xMoS_2	~ MoS_2
	Raman	2H MoS_2/1T MoS_2	1T MoS_2	1T MoS_2
	XPS	2H MoS_2/1T MoS_2	2H MoS_2/1T MoS_2	2H MoS_2/1T MoS_2
Outer	SEM	Flake	Gel Layer	Flake
	XRD	~ MoS_2	Li_2MoO_4	
	Raman	2H MoS_2/1T MoS_2		
	XPS	2H MoS_2/1T MoS_2		1T MoS_2 + SO_x

Fig. 7 Characterisation summary of *ex situ* coloured rings from the ~36 µm thick MoS_2 electrodes cycled to D1 0.80 V (AX), D1 0.01 V (BX), and C1 3.00 V (WX) in a lithium-metal half-cell at a current density of 200 mA g^{-1}.

Conclusions

MoS_2 lithiation in CR2032 coin cells is not uniform but occurs as a lithiation gradient from the outside of the electrode disc moving inwards as electrode contacting deteriorates in the centre. Increasing the electrode coating thickness, causes the lithiation gradient to affect cell performance negatively as the electrode centre stops contributing to electrochemical storage. Therefore, a substantial amount of active material acts as dead mass and results in a lower mass-based performance (~487 mAh g^{-1}) than the theoretical capacity of deep discharge MoS_2 (670 mAh g^{-1}).

Uniting four *ex situ* material characterisation perspectives (SEM, XRD, Raman, and XPS), shows the electrode centre to be almost identical to the pristine 2H MoS_2 electrode, the middle ring to be heterogenous 1T/2H phase Li_xMoS_2/MoS_2, and the outer ring to vary depending on the cutoff voltage (0.80 V, 0.01 V, and 3.00 V). As the cycle progresses, the electrode centre remains mostly unaltered. Within the middle ring 1T/2H phase Li_xMoS_2/MoS_2 forms for all voltages, whereby the MoS_2 structure crystallinity and 2H phase contribution progressively reduces with cycle progression. Nonetheless, the middle ring contains 2H MoS_2, indicating that not all the active material contributes towards the cell storage capacity.

In the outer most ring, the material fully participates in the lithiation mechanism. For the shallow discharge (D1 0.80 V), the region is low crystalline heterogenous 1T/2H phase Li_xMoS_2/MoS_2 with a predominant 1T contribution. On the other hand, the deep discharge (D1 0.01 V) section is covered by a gel-like layer in SEM and is completely amorphous. Therefore, it cannot be penetrated by the Raman laser and is distinguishable with XPS due to sample phase modulation induced by depth-profiling. Following charge (C1 3.00 V), the outer ring remains amorphous, does not exhibit a gel-like layer, and presents weak 1T/2H MoS_2, MoO_3, and sulphate signals in XPS.

In order to avoid further complication of the study of the MoS_2 lithiation mechanism in LIB, we suggest the use of thin coatings (~10 µm) of commercial MoS_2 and the application of low current densities (~10 mA g^{-1}) to enable the coin cell electrodes to uniformly lithiate. Without electrode homogeneity there is an unidentified surplus source of capacity within the cell, considering that not all the MoS_2 present lithiates to deliver ~487 mAh g^{-1}. Additionally, sample inhomogeneities can result in the existence of misleading evidence for competing MoS_2 reaction mechanisms depending on the coloured ring analysed.

In all instances, the cycled electrode surface is dominated by the SEI species fluorine, oxygen, carbon, and lithium (88.9–100.0 at%), which already accounted for most of the surface

(without lithium) even before cell cycling (80.3 at%). Therefore, alongside the study of the MoS_2 lithiation mechanism, the manufacture of well dispersed MoS_2 electrode coatings and the study of MoS_2 LIB SEI layer development should be the focal point of future studies to aid MoS_2 long-term stability without incurring large production or processing costs.

Data availability

Data for this article, including digital images, electrochemical data (.mpt), SEM images, spectroscopy data (Raman & XPS), and XRD diffraction patterns are available at a Science Data Bank repository at **https://www.scidb.cn/en/s/7VBBbu**.

Author contributions

ADM and PLC were responsible for the project conceptualisation. ADM and ARS developed the cell methodology and cycled the cells. ADM collected and analysed the data. ADM wrote the initial draft. ARS, CAH, and PLC reviewed and edited the manuscript.

Conflicts of interest

There are no conflicts to declare.

Acknowledgements

The UK EPSRC (CAH and PLC; EP/S001298/2) and the Faraday Institution (**https://Faraday.ac.uk**; EP/S003053/1) supported this work. The authors (ADM and ARS) would like to acknowledge the Faraday Institution for funding the energy storage work at the Electrochemical Innovation Lab through the LiSTAR (FIRG0014) and Degradation (FIRG001) projects. Additionally, the authors acknowledge the National Physical Laboratory (NPL) for funding the PhD Studentship of ADM.

References

1 K. Abbass, M. Z. Qasim, H. Song, M. Murshed, H. Mahmood and I. Younis, *Environ. Sci. Pollut. Res.*, 2022, **29**, 42539–42559.
2 C. P. Bown, *Peterson Institute for International Economics Working Paper 24-2*, 2024, pp. 1–44.
3 L. S. Martins, L. F. Guimarães, A. B. Botelho Junior, J. A. S. Tenório and D. C. R. Espinosa, *J. Environ. Manage.*, 2021, **295**, 113091.
4 M. Hachhach, H. Akram, M. Hanafi, O. Achak and T. Chafik, *Chem. Prod. Process Model.*, 2023, **18**, 355–368.
5 Y. Deng, J. Li, T. Li, J. Zhang, F. Yang and C. Yuan, *Energy*, 2017, **123**, 77–88.
6 A. D. Marinov, L. Bravo Priegue, A. R. Shah, T. S. Miller, C. A. Howard, G. Hinds, P. R. Shearing, P. L. Cullen and D. J. L. Brett, *ACS Nano*, 2023, **17**, 5163–5186.
7 L. S. Selwyn, W. R. McKinnon, U. von Sacken and C. A. Jones, *Solid State Ionics*, 1987, **22**, 337–344.
8 L. Zhang, D. Sun, J. Kang, J. Feng, H. A. Bechtel, L. W. Wang, E. J. Cairns and J. Guo, *Nano Lett.*, 2018, **18**, 1466–1475.
9 Z. Zhu, Y. Tang, W. R. Leow, H. Xia, Z. Lv, J. Wei, X. Ge, S. Cao, Y. Zhang, W. Zhang, H. Zhang, S. Xi, Y. Du and X. Chen, *Angew. Chem.*, 2019, **131**, 3559–3564.
10 T. Liu, G. Melinte, O. Dolotko, M. Knapp and B. Mendoza-Sánchez, *J. Energy Chem.*, 2022, **78**, 56–70.
11 J. Bai, B. Zhao, J. Zhou, J. Si, Z. Fang, K. Li, H. Ma, J. Dai, X. Zhu and Y. Sun, *Small*, 2019, **15**, 1–11.
12 L. Wang, Q. Zhang, J. Zhu, X. Duan, Z. Xu, Y. Liu, H. Yang and B. Lu, *Energy Storage Mater.*, 2019, **16**, 37–45.
13 K. K. Halankar, B. P. Mandal, M. K. Jangid, A. Mukhopadhyay, N. Abharana, C. Nayak, K. Dasgupta and A. K. Tyagi, *J. Alloys Compd.*, 2020, **844**, 156076.
14 C. Deng, H. Wang and S. Wang, *J. Mater. Chem. A*, 2021, **9**, 15734–15743.
15 K. Leng, Z. Chen, X. Zhao, W. Tang, B. Tian, C. T. Nai, W. Zhou and K. P. Loh, *ACS Nano*, 2016, **10**, 9208–9215.
16 F. Pan, J. Wang, Z. Yang, L. Gu and Y. Yu, *RSC Adv.*, 2015, **5**, 77518–77526.
17 Y. M. Chen, X. Y. Yu, Z. Li, U. Paik and X. W. Lou, *Sci. Adv.*, 2016, **2**, 1–9.
18 Y. Jiao, A. Mukhopadhyay, Y. Ma, L. Yang, A. M. Hafez and H. Zhu, *Adv. Energy Mater.*, 2018, **8**, 1–9.
19 X. Fang, C. Hua, X. Guo, Y. Hu, Z. Wang, X. Gao, F. Wu, J. Wang and L. Chen, *Electrochim. Acta*, 2012, **81**, 155–160.
20 G. Wang, Y. Zhang, H. S. Cho, X. Zhao, F. Kim and J. Zou, *ACS Appl. Energy Mater.*, 2021, **4**, 14180–14190.
21 C. D. Quilty, L. M. Housel, D. C. Bock, M. R. Dunkin, L. Wang, D. M. Lutz, A. Abraham, A. M. Bruck, E. S. Takeuchi, K. J. Takeuchi and A. C. Marschilok, *ACS Appl. Energy Mater.*, 2019, **2**, 7635–7646.
22 X. Fang, X. Guo, Y. Mao, C. Hua, L. Shen, Y. Hu, Z. Wang, F. Wu and L. Chen, *Chem.–Asian J.*, 2012, **7**, 1013–1017.
23 K. Leng, Z. Chen, X. Zhao, W. Tang, B. Tian, C. T. Nai, W. Zhou and K. P. Loh, *ACS Nano*, 2016, **10**, 9208–9215.
24 Q. Su, S. Wang, M. Feng, G. Du and B. Xu, *Sci. Rep.*, 2017, **7**, 7275.
25 L. Wang, Z. Xu, W. Wang and X. Bai, *J. Am. Chem. Soc.*, 2014, **136**, 6693–6697.
26 U. K. Sen, P. Johari, S. Basu, C. Nayak and S. Mitra, *Nanoscale*, 2014, **6**, 10243–10254.
27 Z. Zhu, S. Xi, L. Miao, Y. Tang, Y. Zeng, H. Xia, Z. Lv, W. Zhang, X. Ge, H. Zhang, J. Wei, S. Cao, J. Chen, Y. Du and X. Chen, *Adv. Funct. Mater.*, 2019, **29**(42), 1904843.
28 W. Choi, Y. S. Choi, H. Kim, J. Yoon, Y. Kwon, T. Kim, J. H. Ryu, J. H. Lee, W. Lee, J. Huh, J. M. Kim and W. S. Yoon, *Chem. Mater.*, 2021, **33**, 1935–1945.
29 U. K. Sen, P. Johari, S. Basu, C. Nayak and S. Mitra, *Nanoscale*, 2014, **6**, 10243–10254.
30 L. Wang, Z. Xu, W. Wang and X. Bai, *J. Am. Chem. Soc.*, 2014, **136**, 6693–6697.
31 Z. Zhu, Y. Tang, Z. Lv, J. Wei, Y. Zhang, R. Wang, W. Zhang, H. Xia and M. Ge, *Angew. Chem.*, 2018, **130**, 3718–3722.
32 K. Chang and W. Chen, *Chem. Commun.*, 2011, **47**, 4252.
33 X. Cao, Y. Shi, W. Shi, X. Rui, Q. Yan, J. Kong and H. Zhang, *Small*, 2013, **9**, 3433–3438.

34 Y. Liu, X. He, D. Hanlon, A. Harvey, U. Khan, Y. Li and J. N. Coleman, *ACS Nano*, 2016, **10**, 5980–5990.
35 L. Hu, Y. Ren, H. Yang and Q. Xu, *ACS Appl. Mater. Interfaces*, 2014, **6**, 14644–14652.
36 J. Xiao, X. Wang, X. Yang, S. Xun, G. Liu, P. K. Koech, J. Liu and J. P. Lemmon, *Adv. Funct. Mater.*, 2011, **21**(15), 2840–2846.
37 T. Wang, C. Sun, M. Yang, G. Zhao, S. Wang, F. Ma, L. Zhang, Y. Shao, Y. Wu, B. Huang and X. Hao, *J. Alloys Compd.*, 2017, **716**, 112–118.
38 L. Yang, S. Wang, J. Mao, J. Deng, Q. Gao, Y. Tang and O. G. Schmidt, *Adv. Mater.*, 2013, **25**, 1180–1184.
39 Y. Teng, H. Zhao, Z. Zhang, Z. Li, Q. Xia, Y. Zhang, L. Zhao, X. Du, Z. Du, P. Lv and K. Świerczek, *ACS Nano*, 2016, **10**, 8526–8535.
40 G. Wang, Y. Zhang, H. S. Cho, X. Zhao, F. Kim and J. Zou, *ACS Appl. Energy Mater.*, 2021, **4**, 14180–14190.
41 W. Xie, Z. Zhang and X. Gao, *Electrochim. Acta*, 2024, **493**, 144396.
42 S. K. Das, R. Mallavajula, N. Jayaprakash and L. A. Archer, *J. Mater. Chem.*, 2012, **22**, 12988–12992.
43 K. N. Wood and G. Teeter, *ACS Appl. Energy Mater.*, 2018, **1**, 4493–4504.
44 M. A. Baker, R. Gilmore, C. Lenardi and W. Gissler, *Appl. Surf. Sci.*, 1999, **150**, 255–262.
45 N. H. Attanayake, A. C. Thenuwara, A. Patra, Y. V. Aulin, T. M. Tran, H. Chakraborty, E. Borguet, M. L. Klein, J. P. Perdew and D. R. Strongin, *ACS Energy Lett.*, 2018, **3**, 7–13.
46 W. Chen, J. Gu, Q. Liu, R. Luo, L. Yao, B. Sun, W. Zhang, H. Su, B. Chen, P. Liu and D. Zhang, *ACS Nano*, 2018, **12**, 308–316.
47 M. Acerce, D. Voiry and M. Chhowalla, *Nat. Nanotechnol.*, 2015, **10**, 313–318.
48 M. Wahlqvist and A. Shchukarev, *J. Electron Spectrosc. Relat. Phenom.*, 2007, **156–158**, 310–314.
49 Z. Wang, Y. Dong, H. Li, Z. Zhao, H. Bin Wu, C. Hao, S. Liu, J. Qiu and X. W. D. Lou, *Nat. Commun.*, 2014, **5**, 5002.
50 A. Santoni, F. Rondino, C. Malerba, M. Valentini and A. Mittiga, *Appl. Surf. Sci.*, 2017, **392**, 795–800.
51 S. Bae, N. Sugiyama, T. Matsuo, H. Raebiger, K. I. Shudo and K. Ohno, *Phys. Rev. Appl.*, 2017, **7**, 1–7.
52 R. Addou, S. McDonnell, D. Barrera, Z. Guo, A. Azcatl, J. Wang, H. Zhu, C. L. Hinkle, M. Quevedo-Lopez, H. N. Alshareef, L. Colombo, J. W. P. Hsu and R. M. Wallace, *ACS Nano*, 2015, **9**, 9124–9133.
53 J. Luxa, V. Mazánek, A. Mackova, P. Malinsky, S. Akhmadaliev and Z. Sofer, *Appl. Mater. Today*, 2019, **14**, 216–223.
54 L. H. Isherwood, Z. Hennighausen, S. K. Son, B. F. Spencer, P. T. Wady, S. M. Shubeita, S. Kar, C. Casiraghi and A. Baidak, *2D Mater.*, 2020, **7**(3), 035011.
55 T. Grünleitner, A. Henning, M. Bissolo, M. Zengerle, L. Gregoratti, M. Amati, P. Zeller, J. Eichhorn, A. V. Stier, A. W. Holleitner, J. J. Finley and I. D. Sharp, *ACS Nano*, 2022, **16**, 20364–20375.